Electronic Supplementary Information (ESI)

Controllable nanothorns on TiO_2 mesocrystals for efficient charge separation in hydrogen evolution

Peng Zhang, Sooyeon Kim, Mamoru Fujitsuka and Tetsuro Majima*

The Institute of Scientific and Industrial Research (SANKEN), Osaka University, Mihogaoka 8-1, Ibaraki, Osaka 567-0047, Japan

1. Material synthesis

Materials. Titanium(IV) fluoride, chloroplatinic acid, and anatase TiO_2 nanoparticles (Nano) were purchased from Sigma-Aldrich. Ammonium nitrate, ammonium fluoride, boric acid, and methanol were purchased from Wako Pure Chemical Industries. All chemicals were of analytical grade and used as received.

Preparation of TMC-101. The samples were synthesized according to the previous reports with some modifications.[S1] A thin film of precursor solution containing TiF_4, H_2O, NH_4NO_3, and NH_4F (molar ratio = 1:117:6.6:4) was annealed on a silicon wafer in air at a heating rate of 10 ^oC min^{-1} to 160 ^oC for 2 h. The annealed samples were collected and mixed with boric acid (0.5 M) at 60 ^oC for 4 h and dried after washing by water and ethanol separately. [S2] The obtained samples were treated with NaOH aqueous solution (0.01 M) in the dark for 8 h to remove the excess fluorine impurity [S3] and subsequently calcined at 500 ^oC for 2 h, which was referred as TMC-101. TMC-001, a reference sample, was prepared by calcination at 500 ^oC for 2 h after washing with boric acid without the NaOH treatment.

Preparation of Pt/TMC-101 and other samples. Pt nanoparticles (1 wt%) were photochemically deposited on TMC and Nano.[S4] In a typical procedure, 30 mg catalyst, 27 mL of Milli-Q ultrapure water (Millipore), 3 mL methanol, and a certain amount H_2PtCl_6 were mixed to form a homogeneous suspension. The suspensions

were then exposed to the UV-LED source (Asahi Spectra, POT-365; 100 mW cm^{-2}) for 30 min at room temperature. The products were collected after centrifugation and drying. The amounts of loaded Pt were determined by inductively coupled plasma emission spectroscopy (Shimadzu, ICPS-8100).

2. Characterizations. Structures of the samples were characterized by X-ray diffraction (XRD, Rigaku Rint-2500, CuKα source). Morphologies were examined by scanning transmission electron microscopy (STEM) equipped with energy dispersive spectroscopy (EDS) mapping using JEM-ARM200F microscope operated at 200 kV. The steady-state UV-visible absorption and diffuse reflectance spectra were measured by UV-visible-NIR spectrophotometers (Shimadzu, UV-3100 and Jasco V-570, respectively) at room temperature. The Brunauer–Emmett–Teller (BET) surface areas were measured using nitrogen adsorption (BEL Japan, BELSORP max). The pore volumes and diameter distributions were derived from the adsorption isotherms using the Barrett–Joyner–Halenda (BJH) model. Photoelectrochemical measurements were carried out in a conventional three-electrode cell using an electrochemical station (ALS, model 660A). The photocatalyst was drop casted on a glassy carbon working electrode, and Pt wire and Ag/AgCl in a saturated KCl solution were used as a counter a reference electrode, respectively. 0.5 M Na_2SO_4 was used as the electrolyte in aqueous solution (pH~6.4).

3. Photocatalytic H_2 Generation Tests. Approximately 2 mg of photocatalyst was suspended in a 2 mL water solution containing methanol (20 vol%) in a 10 mL quartz cell. The cell was sealed with a rubber septum and purged with Ar gas for 20 min before the irradiation. The sample was irradiated using UV-LED source (Asahi Spectra, POT-365; 100 $mWcm^{-2}$) with constant magnetic stirring at room temperature. After the reaction, 0.1 mL of the gas was collected from the headspace of the reactor and analyzed using a Shimadzu GC-8A gas chromatograph equipped with an MS-5 A column and a thermal conductivity detector.

4. Sample Preparation for Single-Particle PL Experiments. The quartz cover glasses were purchased from Matsunami Glass and cleaned by sonication in a 20 % detergent solution (Cleanace, As One) for 6 h, followed by washings with warm water for 5 times. Finally, the quartz cover glasses were washed again with Milli-Q ultrapure water (Millipore). The suspension with a low concentration of different samples were spin-coated on the pre-cleaned quartz cover glass, which was subsequently annealed at 100 °C for 0.5 h to immobilize the particles on the glass surface.

5. Single-Particle PL Measurements by Confocal Microscopy. Single-particle PL images and spectra were recorded by using an objective scanning confocal fluorescence microscope system (PicoQuant, MicroTime 200). The samples were excited through an oil-immersion objective lens (Olympus, UplanSApochromat, 100×, 1.4 NA) with a circular-polarized 375-nm pulsed laser (Spectra-Physics, Mai Tai HTS-W with an automated frequency doubler, Inspire Blue FAST-W; 0.8MHz repetition rate) controlled by a PDL-800B driver (PicoQuant). The emission from the sample was collected by the same objective and detected by a single-photon avalanche photodiode (Micro Photon Devices, PDM 50CT) through a dichroic beam splitter (Chroma, z405rdc) and long pass filter (Chroma, HQ435CP). For the spectroscopy, only the emission that passed through a slit was detected with the imaging spectrograph (Acton Research, SP-2356) equipped with an electron-multiplying charge-coupled device (EMCCD) camera (Princeton Instruments, ProEM).

6. Time-Resolved Transient Absorption Measurements. The femtosecond transient absorption spectra were measured by the pump and probe method using a regenerative amplified titanium sapphire laser (Spectra-Physics, Spitfire Pro F, 1 kHz). The output of the optical parametric amplifier (330 nm, 3 μJ $pulse^{-1}$, Spectra-Physics, OPA-800CF-1) was used as the excitation pulse. A white continuum pulse was generated by focusing the residual of the fundamental light on a sapphire crystal and detected by

a linear InGaAs array detector equipped with the polychromator (Solar, MS3504). All measurements were carried out at room temperature.

7. Supplementary Tables and Figures.

Table S1. Structural characteristics of NH_4TiOF_3, porous TiO_2, and TMC-101.

Sample	S_{BET} ($m^2\ g^{-1}$)	V_p ($cm^3\ g^{-1}$)	D_p (nm)	Particle size (nm)
NH_4TiOF_3	11	0.04	1.2	-
Porous TiO_2	106	0.11	5.0	6
TMC-101	35	0.14	12.0	12

Table S2. XPS peak positions of the elements in NH_4TiOF_3, porous TiO_2, TMC-001, and TMC-101.

Sample	Ti $2p_{3/2}$ (eV)	O 1s (eV)	F 1s (eV)	N 1s (eV)
NH_4TiOF_3	460.3	530.9	684.8	402.5
Porous TiO_2	459.5	530.7	684.8	-
TMC-001	459.5	530.7	684.8	-
TMC-101	459.5	530.7	684.8	-

Table S3. Kinetic parameters of the emission decay of porous TiO_2 and TMC-101.[a]

Sample	Position	τ_1 (ns)	τ_2 (ns)	τ_3 (ns)	$\langle\tau_{PL}\rangle$[b] (ns)
Porous TiO_2	center	0.17	0.66	2.6	1.1
	edge	0.16	0.60	2.3	1.0
TMC-101	center	0.20	0.66	3.2	1.4
	edge	0.26	0.95	3.9	1.7

[a]The multiexponential decay curves were fitted using a nonlinear least-squares method with a multicomponent decay given by $I(t) = a_1 \cdot \exp(-t/\tau_1) + a_2 \cdot \exp(-t/\tau_2) + \cdots + a_n \cdot \exp(-t/\tau_n)$.

[b]The average lifetime $\langle\tau_{PL}\rangle$ was determined using the following equation.

$$\langle \tau_{PL} \rangle = \sum_{i=1}^{i=n} a_i \tau_i^2 / \sum_{i=1}^{i=n} a_i \tau_i$$

Table S4. Kinetic parameters of transient absorption decays.

Sample	τ_1 (ps)	τ_2 (ps)	τ_3 (ps)
Nano	12 ± 1.4 (21%)	46 ± 14 (34%)	590 ± 120 (45%)
Porous TiO_2	5.0 ± 0.6 (32%)	54 ± 3.3 (37%)	550 ± 36 (31%)
TMC-001	16 ± 1.3 (30%)	90 ± 8.0 (38%)	620 ± 72 (32%)
TMC-101	14 ± 1.2 (24%)	110 ± 8.2 (39%)	900 ± 100 (37%)

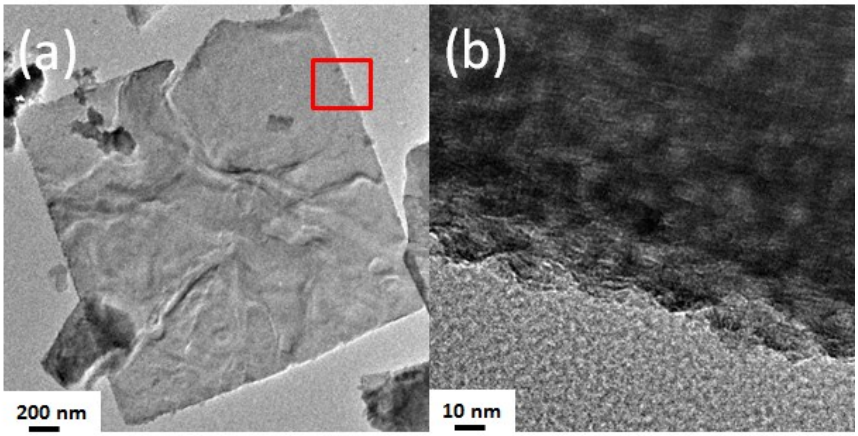

Fig. S1 (a) TEM image of NH_4TiOF_3 and the red-square place in (a) is magnified to (b).

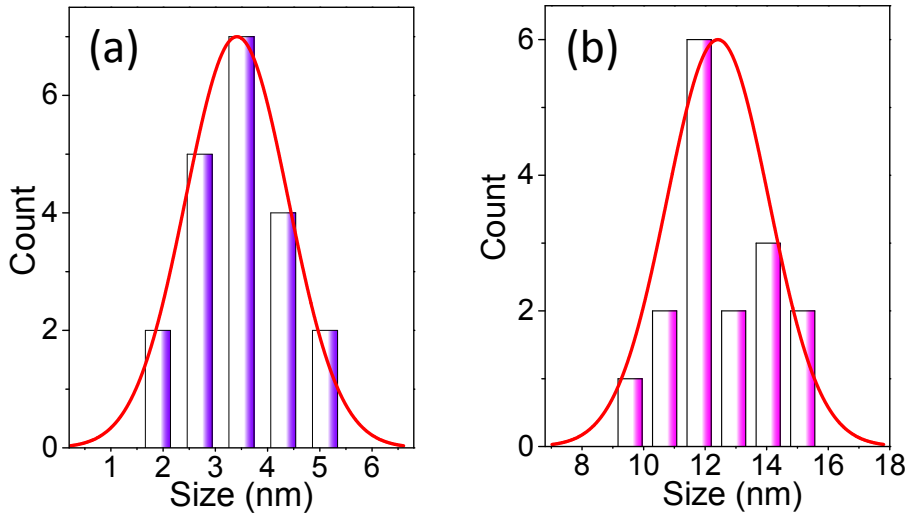

Fig. S2 Size distribution of (a) porous TiO_2 and (b) TMC-101 observed from the corresponding TEM images. The curves are obtained by Gaussian fitting.

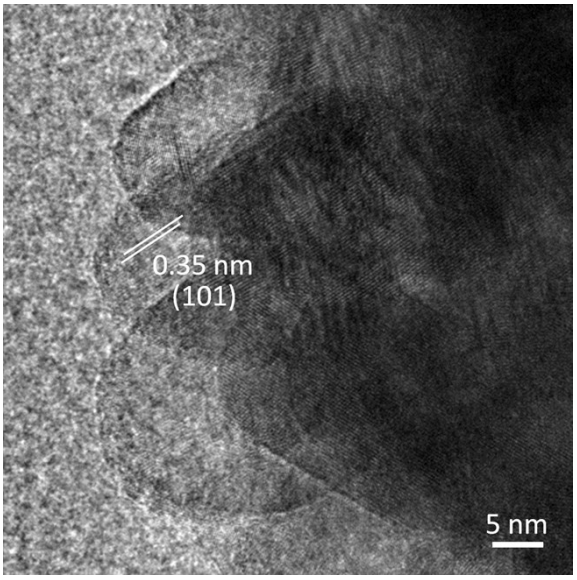

Fig. S3 HRTEM image of the lateral facet of TMC-101 from Fig. 2f.

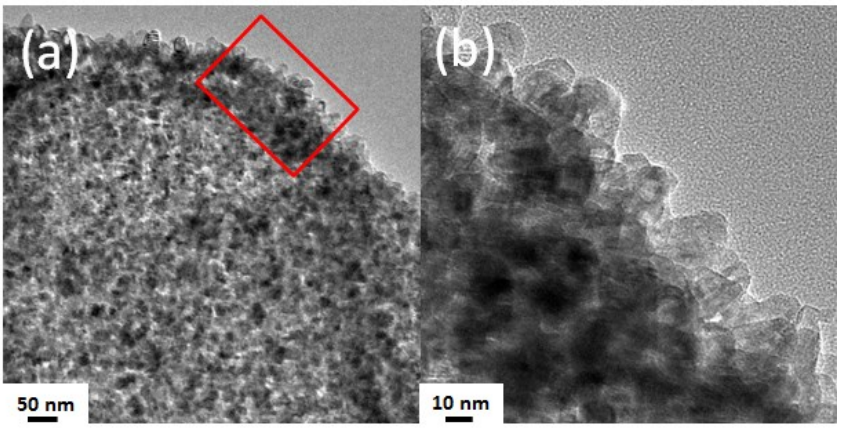

Fig. S4 HRTEM image of the broken part of TMC-101 (a) from Fig. 2f and the red-square place in (a) is magnified to (b).

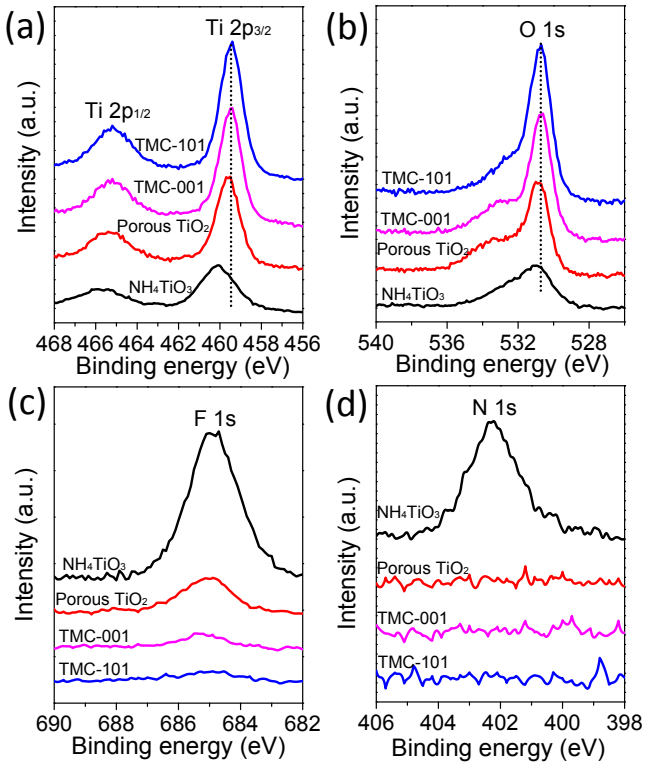

Fig. S5 Comparison of XPS spectra of Ti 2p (a), O 1s (b), F 1s (c), and N 1s (d) in the series of NH_4TiOF_3, porous TiO_2, TMC-001, and TMC-101.

The relative elemental composition during the growth process was analyzed using high-resolution XPS (Table S2 and Fig. S5, ESI†). To clarify the effect of residual fluorine on the predominant morphology, the reference (TMC-001) with dominant {001} facet (Fig. S6, ESI†) was prepared without the NaOH treatment. NH_4TiOF_3 phase and series of TiO_2 phase were confirmed by peaks of Ti 2p and O 1s. The peaks of Ti $2p_{3/2}$ and Ti $2p_{1/2}$ (Fig. S5a, ESI†) and O 1s (Fig. S5b, ESI†) shifted due to topotactic transformation from NH_4TiOF_3 to porous anatase TiO_2, TMC-001, and TMC-101 (Table S2, ESI†). As shown in Fig S5c, apparent F 1s peak around binding energy of 684.8 eV in all samples can be attributed to fluorine adsorbed or substituted on surface.[S1] Intriguingly, the negligible peaks of N 1s (Fig. S5d, ESI†) were observed with porous TiO_2, TMC-001, and TMC-101, but not with NH_4TiOF_3, indicating that the elemental N was removed from NH_4TiOF_3 after the H_3BO_3 treatment. The NaOH treatment had a significant effect on the content of residual fluorine in samples. When compared to the initial intermediate of NH_4TiOF_3, as well as porous TiO_2, both TMC-001 and TMC-101 showed much weaker intensity of fluorine. The residual fluorine in TMC-001, originally from porous TiO_2, was more than in TMC-101 even after the annealing, which is consistent with crystal growth along (001) axis during the topotactic transformation. However, the annealing at elevated temperature always gave rise to the doping process on TMC-001.[S1]

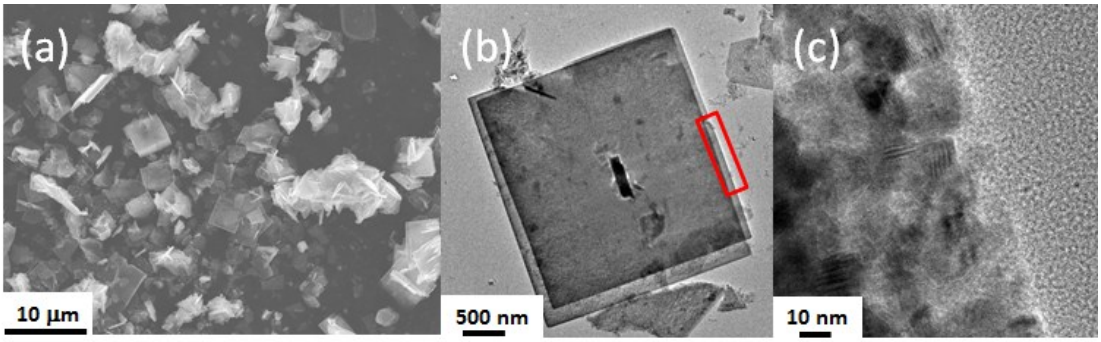

Fig. S6 (a) FESEM and (b) TEM images of TMC-001, and the red-square place in (b) is magnified to (c).

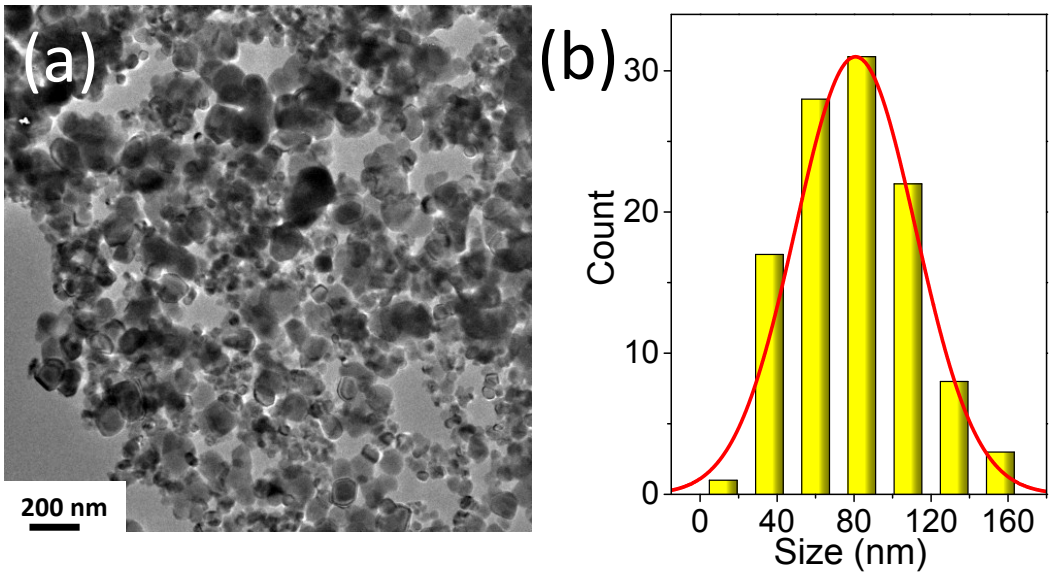

Fig. S7 (a) TEM image and (b) size distribution of the benchmark (Nano).

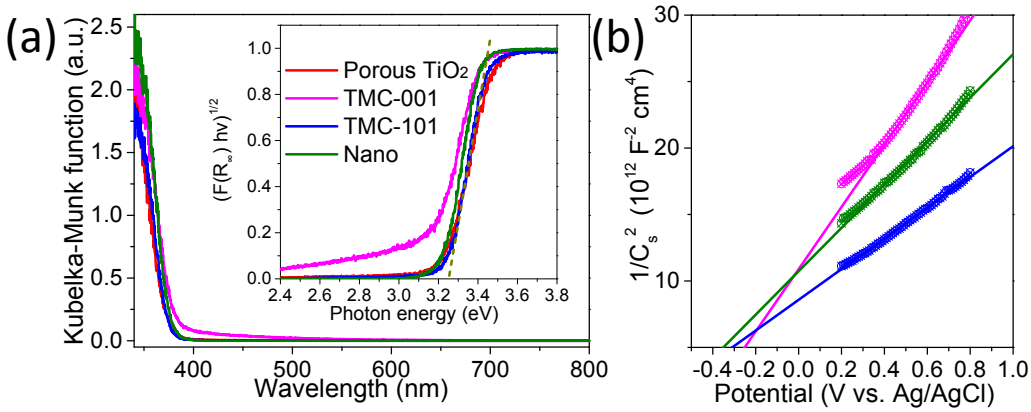

Fig. S8 (a) Steady-state diffuse reflectance spectra and (b) the corresponding of Mott-Schottky plots from the series of porous TiO_2, TMC-101, TMC-001, and Nano. The inset in (a) is *Tauc* plot.

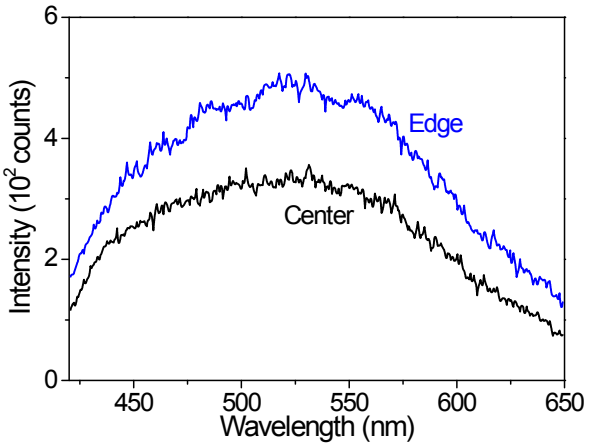

Fig. S9 Emission spectra observed at the center and edge positions of TMC-101.

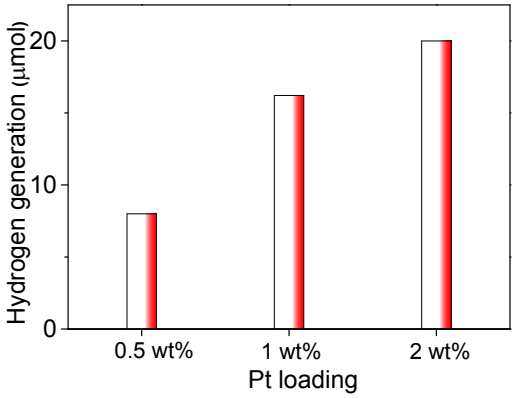

Fig. S10 Hydrogen generation on TMC-101 with different loading of Pt.

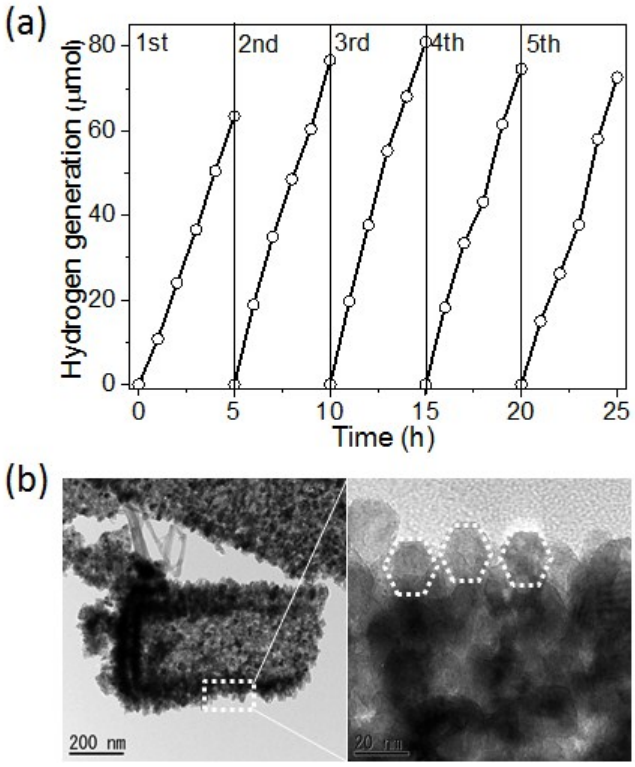

Fig. S11 The stability of Pt/TMC-101 in H_2 evolution after 5 cycles (a) and its corresponding structure in TEM (b).

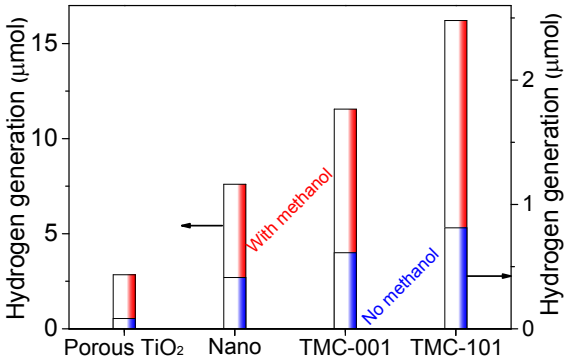

Fig. S12 The effect of sacrificial agent on the H_2 generation from different samples.

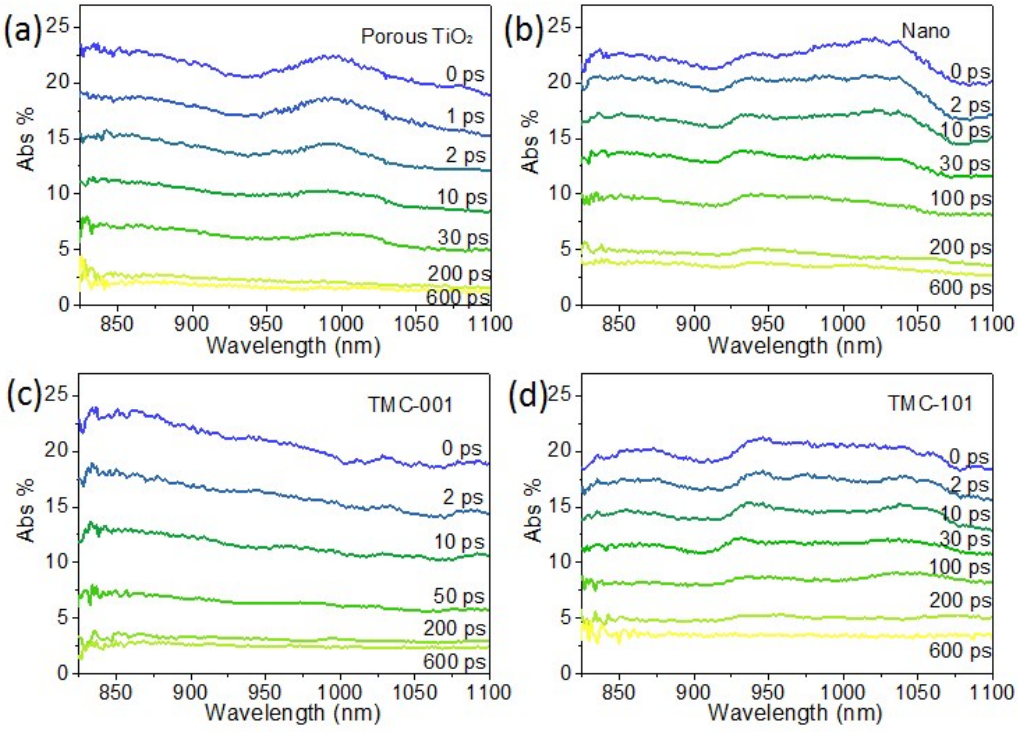

Fig. S13 Transient absorption spectra of (a) porous TiO_2, (b) Nano, (c) TMC-001, and (d) TMC-101 in the time scale of 0~600 ps.

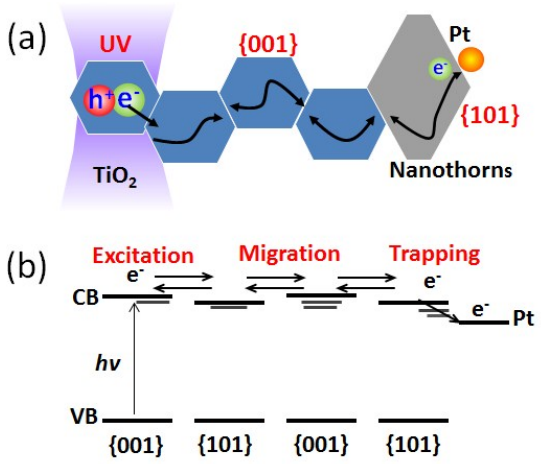

Fig. S14 Illustration of (a) the anisotropic electron flow between facets and (b) band gap excitation, showing electron migration through {001} and {101} facets, and electron trapping to the trap cite (Pt nanoparticle).

It is well known that TiO_2 superstructure with ordered nanocrystals separates photogenerated charges more efficiently than disordered nanoparticles, and thus attractive for enhancing the photocatalytic activity.[S5] In our case, TMC-101 exhibited superior activity due to the specific facet-induced anisotropic electron flow along the long-range interparticles and charge separation between the adjacent {001} and {101} facets (Fig. S14a, ESI†). From the previous work, it has been clearly demonstrated that the dominant facets can shift both band gap and band edges of photocatalyst.[S6] Tauc plot and flat potential measurements indicated that the band edge of TMC-101 was more positive than TMC-001. From different electronic band structures of facets, the anisotropic electron flow occurs between facets. In the case of TMC-101 (Fig. S14b, ESI†), after band gap excitation, the specific facet-induced charge migration and trapping/detrapping between dominant {101} and minor {001} facets proceed through the trap states under the conduction band to some extent. The Pt nanoparticles, preferably photodeposited on nanothorns with dominant {101} facet, capture the migrated electrons to cause the efficient HER. That is the main reason explaining why TMC-101 exhibited superior activity than others.

References

(S1) P. Zhang, M. Fujitsuka, T. Majima, *Appl. Catal., B* 2016, **185**, 181.
(S2) L. Zhou, D. Smyth-Boyle, P. O'Brien, *J. Am. Chem. Soc.* 2008, **130**, 1309.
(S3) T. R. Gordon, M. Cargnello, T. Paik, F. Mangolini, R. T. Weber, P. Fornasiero, C. B. Murray, *J. Am. Chem. Soc.* 2012, **134**, 6751.
(S4) P. Zhang, T. Tachikawa, Z. Bian, T. Majima, *Appl. Catal., B* 2015, **176–177**, 678.
(S5) P. Zhang, M. Fujitsuka, T. Majima, *J. Energy Chem.* 2016, **25**, 917.
(S6) J. Pan, G. Liu, G. Q. Lu, H. M. Cheng, *Angew. Chem., Int. Ed.* 2011, **50**, 2133.